HHS Public Access

Author manuscript

Adv Mater. Author manuscript; available in PMC 2018 March 01.

Published in final edited form as:

Adv Mater. 2017 March ; 29(11): . doi:10.1002/adma.201605416.

Paramagnetic properties of metal-free boron-doped graphene quantum dots and their application for safe magnetic resonance imaging

Dr. Hui Wang,
Department of Materials Science and Engineering, University of Washington, Seattle, Washington 98195 (United States)

Mr. Richard Revia,
Department of Materials Science and Engineering, University of Washington, Seattle, Washington 98195 (United States)

Dr. Kui Wang,
Department of Materials Science and Engineering, University of Washington, Seattle, Washington 98195 (United States)

Mr. Rajeev J Kant,
Department of Materials Science and Engineering, University of Washington, Seattle, Washington 98195 (United States)

Dr. Qingxin Mu,
Department of Materials Science and Engineering, University of Washington, Seattle, Washington 98195 (United States)

Dr. Zheng Gai,
Center for Nanophase Materials Sciences and Chemical Science Division, Oak Ridge National Laboratory, Oak Ridge, Tennessee 37831 (United States)

Dr. Kunlun Hong, and
Center for Nanophase Materials Sciences and Chemical Science Division, Oak Ridge National Laboratory, Oak Ridge, Tennessee 37831 (United States)

Prof. Miqin Zhang
Department of Materials Science and Engineering, University of Washington, Seattle, Washington 98195 (United States)

Abstract

The study introduces a boron-doped graphene quantum dot (B-GQD) as a metal-free multi-modal contrast agent (CA) for safe MRI and fluorescence imaging. *In vivo* T_1-weighted MR images shows B-GQDs induce significant contrast enhancement on heart, liver, spleen and kidney and sustain for more than 1 h, about 10 times longer than Gd-based CAs currently used in clinic.

Correspondence to: Miqin Zhang.

Supporting Information

Supporting Information is available from the Wiley Online Library or from the author.

Graphical Abstract

Keywords

Metal-free; boron-doping; graphene quantum dot; paramagnetism; MRI

Metal-free carbon-based magnetic materials (MFCMMs) have been a research frontier in physics, chemistry, and materials science since the discovery of ferromagnetism in tetrakis(dimethylamino)ethylenefullerene.[1, 2] Due to their appealing attributes including long coherence time, quantum effects, negative differential conductance, complete current suppression, and biocompatibility, the synthesis and potential applications of MFCMMs with macroscopic magnetic ordering are both fundamentally and technologically important.[3–5] Early theoretical studies revealed the ferromagnetic property of metal-free (MF) graphene due to the presence of various defects in the material such as vacancies, topological defects, modification of the crystal lattice, as well as hydrogen chemisorption.[6–9] Several subsequent studies have confirmed the ferromagnetism and paramagnetism in graphene, reduced graphene oxide, and graphite,[10–14] but no study has reported the magnetic properties of graphene quantum dots (GQDs) that may potentially serve in many magnetism-related applications such as magnetic resonance imaging (MRI) in particular.

MRI is a non-invasive, sensitive, and preferred imaging modality in clinic due to its high spatial resolution and virtually unlimited tissue penetration depth.[15, 16] Unlike X-ray computer Tomography (CT) and position emission tomography (PET) scans, MR imaging does not use ionizing radiation that may cause harmful side effects. Paramagnetic complexes containing gadolinium (Gd-based contrast agents) have been widely used as T_1 positive contrast agents (brightening signaling) for MRI in clinic for decades and exhibit better spatial resolution and diagnosis of medical conditions than T_2 negative contrast agents (darkening signaling). Paramagnetic nanoparticles (NPs) have been extensively investigated in the past decade as potential contrast agents (CA)s for MRI to overcome the limitation of the short half-life and low sensitivity of Gd-based contrast agents. However, these Gd-based CAs pose some safety concerns for their possible association with renal failure and nephrogenic systemic fibrosis (NSF), and may cause excess metal deposits, and other susceptibility artifacts.[17–20] Although encapsulation of metal-based CAs in mesoporous nanocarriers has been an alternative approach that can temporarily suppress the metal release to reduce toxicity, the subsequent degradation of the encapsulating material may still release metal to the surroundings, leading to side effects to the body.[21] Furthermore, the food and drug administration (FDA) has recently issued a safety alert about the possible long-term deposition of Gd-based contrast agents in brain tissue.[22] Thus there is an urgent demand for development of non-metal MRI contrast agents that exhibit sensitivity and functionalities comparable or superior to existing T_1 contrast agents.

Here, we report the developemnt of metal-free boron-doped graphene quantum dots (B-GODs) as a safe T_1 contrast agent for MRI. This meganetic properties is produced by introducing both vacancies and elemental boron molecules as the substitutional defect. The B-GQDs were synthesized at 200°C using 4-vinylphenylboronic acid (VPBA) and with boric acid as the precursor. The formation of B-GQDs (Figure 1a) involves two steps. First, VPBA molecules form the polymer by breaking carbon-carbon double bonds under high pressure and temperature; H_2O_2 decomposes to form free radicals of hydroxyl (HO·) and hydroperoxyl (HOO·) and subsequently O_2 and H_2O. Second, the chemical bonds of C–H and benzene ring in the polymer and O–B in boric acid are ruptured to form boron-doped carbon-based free radicals and then larger carbon-based fragments. The hydroxyl and hydroperoxyl react with the carbon-based free radicals to form hydrophilic hydroxyl and carboxyl groups. The pressure increase caused by the produced O_2 and H_2O furtherpromotes the reaction to form crystallized graphene quantum dots (GQDs). Further, defects in the GQD framework provides active sites for boron doping by decomposition of VPBA and boric acid, thus leading to the formation of B-GQDs by a nuclear burst at the supersaturation point.

The TEM image in Figure 1b shows that the produced B-GQDs are well dispersed and have an average size of ~ 5.8 nm. High-resolution TEM image (Figure 1c) shows that B-GQDs have a crystalline structure with an interplanar distance of ~0.321 nm, corresponding well to the (002) lattice planes of graphene.[23] The thickness of B-GQDs was characterized by atomic force microscope (AFM). As shown in Figure 1d, B-GQDs have a height distribution peacked at ~3 nm. The crystallographic structure and phase purity of B-GQDs were examined by XRD and Raman scattering techniques, respctively. The characteristic peak of 002 in the XRD pattern (Figure S1, Supporting Information) can be indexed to the bulk graphite.[24] The high-degree graphitization is also confirmed by the Raman spectrum (Figure 1e), where the sginal of the ordered G band at 1587 cm^{-1} is stronger than the signal of the disordered D band at 1362 cm^{-1} with a large G to D intensity ratio of 1.1.[25] Further, the D-mode at 1362 cm^{-1} in the Raman spectrum also indicates the presence of vacancy defects in B-GQDs. The XPS survey and high resolution spectra of C1s, O1s, and B1s (Figure S2, Supporting Information) show that carbon (69.23%), oxygen (23.64%) and boron (7.23%) are present on the surface of B-GQDs. No metal peaks were found in XPS spectra, confirming the metal-free of B-GQDs. B1s peaks at 190.9 and 191.8 eV indicate the presence of sp^2 C=B bonds, confirming the successful doping of boron in GQDs.

The UV–Vis absorption spectrum (Figure S3, Supporting Information) of B-GQDs shows an absorption band at ~244 nm resulted from **π**-**π*** transition of aromatic domains in B-GQDs.[26, 27] A shoulder peak at 272 nm is observed, which is attributable to n-**π*** transition of C=O bonds and characteristic absorption peak of GQDs.[28] A detailed photoluminescence (PL) study of B-GQDs was carried out under different excitation wavelengths. As shown in Figure 1g and f, B-GQDs demonstrate an excitation wavelength-tunable and upconverted fluorescence property, suggesting that B-GQDs could serve as an optical imaging contrast agent with a broad range of wavelength from ultraviolet to NIR light.[29] The photoluinescence (PL) quantum yield of B-GQDs was determined to be 11.2% using rhodamine B as a standard. This tunable PL property (emission wavelength and intensity) of B-GQDs can be attributed to the quantum confinement of conjugated **π**-

electrons in an sp^2 network, the presence of defects (including heteroatom doping), multiphoton active processes and potential anti-stokes transition.[30–33] The hydrophilic carboxyl groups including O-H stretching at 3428 cm^{-1} and C=O stretching mode at 1701 cm^{-1} (Figure S4, Supporting Information) on the surface of B-GQDs endow them good water-solubility (Figure 1b, inset).

Magnetism of B-GQDs was assesed with a superconducting quantum interference device magnetometer (SQUID). Great care was taken during the preparation of B-GQDs to ensure that there were no metal impurities. The samples for SQUID were first assessed by inductively coupled plasma atomic emission spectroscopy (ICP-AES). Results show that no Gd, Fe, Co and Mn elements are present in B-GQDs (not shown) which may otherwise also contribute to the paramagneism. Figure 2a shows the field sensitive temperature dependence of magnetization measured at fields of 50 Oe in both the zero field cooled (ZFC) and field cooled (FC) states. The magnetic moments monotonically increase with decreasing temperature down to 5 K. The steep increase in magnetization at low temperatures indicates the strong paramagnetic behavior of B-GQDs.[34, 35] The comparison of the magnetic hysteresis (M–H) curves at 6K and 300K in Figure 2b confirms the strong paramagnetic behavior of B-GQDs which have a magnetization value of 2.935 emu/g and 0.0398 emu/g, respectively, at these two temperatures.

It is worth mentioning that the magnetization value of B-GQDs is lower than those of paramagnetic lanthanide oxide NPs (e.g., Gd_2O_3, 6.25 emu/g; Eu_2O_3, 1.38 emu/g) at 300 K,[36] but, as mentioned above, metal-containing materials pose a safety concern for medical applications. On the other hand, most metal-free graphene-based materials with defects demonstrate a ferromagnetic property at 300 K. However, materials with ferromagnetic properties cannot serve as positive T_1 CAs.[37–42] Metal-free graphite and metal-free graphene oxide could also produce paramagnetism by introducing dipolar C-F bonds.[43, 44] For example, it has been reported that graphite doped with fluorine demonstrates a paramagnetic property (0.82 emu/g). However, application of these materials in medicine is limited by potential toxicity, poor stability, high uptake by liver, and low tissue penetration depth primarily due to their larger sizes (1 μm).[44]

Figure S5 (Supporting Information) shows the Curie-Weiss law fitting (M = c*H/T) of the paramagnetic component of B-GQDs with a Curie constant of 6.25×10^{-4}. To investigate the influence of boron doping on the magnetism of GQDs, pure GQDs were prepared as a control using a sythesis method similar to the method for synthesizing B-GQDs (Figure S6 and Figure S7, Supporting Information). Compared to B-CQDs (Figure 2a), GQDs display weak diamagnetism (Figure S8, Supporting Information), which indicates that the boron doping can induce the transition of GQDs from weak diamagnetism to paramagnetism. The paramagnetism of B-GQDs may be attributed to the local magnetic moments of dangling bonds.[45] Such a bond may produce a localized spin and further convert a graphite sp^2 bond into an sp^3 bond at the expense of a π bond. Localized spins in a high boron concentration region behave like isolated spins, therefore, leading to the formation of paramagnetic centers.[46]

Given their paramagnetic behavior, B-GQDs were investigated as a T_1 CA for MRI both *in vitro* and *in vivo*. As shown in Figure 2c, the T_1 signal intensity increases with increasing B-GQD concentration (corresponding to an increase in carbon concentration). This indicates the capability of our MF B-GQDs to enhance contrast in T_1-weighted MRI. T_1 values were then plotted as $1/T_1$ as a function of carbon molar concentration (Figure 2d). The relaxation ($1/T_1$) exhibits a linear relationship with carbon molar concentration, and the longitudinal relaxivity, r_1 (the slope of the best fit line in this linear relation) of B-GQDs is 18.277 mM^{-1} s^{-1} (Figure 3b). Comparatively, the r_1 of GQDs is only 0.0038 mM^{-1} s^{-1} (Figure S9, Supporting Information), indicating that the boron doping of GQDs substantially increase the longitudinal relaxivity. Also notably, although the magnetization value of B-GQDs is lower than paramagnetic lanthanide oxide NPs as mentioned above, the r_1 relaxivity of B-GQDs is much greater than these metal-based T1 CAs (Gd_2O_3, 4.25 mM^{-1} s^{-1}; Eu_2O_3, 0.006 mM^{-1} s^{-1}).[36] In addition, the r_1 relaxivity of B-GQDs is also much greater than the relaxivity of the most commonly-used clinical T_1 CA (i.e., Gd-DTPA, r_1 = 5.39 mM^{-1} s^{-1}, Figure S10, Supporting Information). Further, although it is reported that the introducing Gd into carbon dots could inrease the relaxivity of carbon dots,[47,48] the r_1 relaxivity of B-GQDs is still greater than that of reported Gd-carbon dots (r_1 = 11.35 mM^{-1} s^{-1}).[49] This suggests that the boron doping is more efficient than metal doping in carbon-based materials in enhancing the relaxivity. This may be due to the smaller diameter of doped boron atoms that produce more paramagnetic centers in nanostructured carbon materials. Our B-GQDs are the first metal-free contrast agent that provides contrast enhancement in T_1-weighted imaging and may have a significant implication in medical imaging.

The cytotoxicity of B-GQDs were evaluated with two tumor cell lines (SF763 and BT474) and one healthy cell line (HEK293T). More than 96% of cells from all three cell lines survived 72 h after treatment with B-GQDs at different concentrations. This indicates that B-GQDs are nontoxic to the tested cells (Figure 3a).

The biodistribution of B-GQDs were evaluated by injecting B-GQDs into wild-type of mice and quantifying the fluorescence intensities of B-GQDs in organs of interest (Figure 3b). Results showed significant portions of B-GQDs were taken up by liver, stomach and spleen while lesser amounts were found in lung and heart at 72 h post injection. B-GQDs showed no obvious systemic toxicity as demonstrated by assays of serum markers of liver and kidney functions (Figure 3c and d). As shown in Figure 3c and d, the levels of serum alanine aminotransferase, white blood cells, platelet, and blood urea nitrogen were similar between PBS and B-GQD treated animals, suggesting that B-GQDs do not induce liver toxicity at the given dosage despite the large accumulation of B-GQDs in liver.[50] The biocompatibility of B-GQDs *in vivo* was assessed by histological analysis of various tissues from mice treated by intravascular injection with B-GQDs or PBS solution (as control). The analysis of tissue sections showed that the tissues from the mice receiving B-GQDs appear similar to those from control animals (receiving PBS), and no evidence of toxicity was observed (Figure 3e).

To evaluate the MRI imaging capability of B-GQDs in mice, B-GODs were administered with B-GQDs through subcutaneous injection. As shown in Figure S11 (Supporting information), B-GQDs demonstrated a substantial contrast enhancement as compared to PBS-injected solution. The contrast enhancement by B-GQDs was further assessed by

intravenous injection of 100 μL dispersive PBS solution containing B-GQDs (0.2 mg) into wide-type mice. T_1-weighted MR images of the cross-section views of mice centered on heart, liver, kidney, stomach, and spleen (Figure 4a) were acquired before and after the injection. The signal intensity of positive contrast increased over time throughout the duration of the experiment (68 min) in all organs, followed by a weak decay at the end of the experiment (about 90 min). In these T_1-weighted images, heart and stomach show higher positive contrast enhancement than kidney, spleen, and liver. Quantitatively, the T_1 signal intensity (Figure 4b) was increased by 403.4% and 522.4% for heart and stomach, respectively, at 93 min post-injection, relative to the signal intensities of these of these organs before the injection. The enhanced signal sustains for more than 1.5 h (consistent with the blood half-life of B-GQDs in Figure 4c), which is seven times longer than a commonly-used Gd-based clinical MRI T1 CA (<10 min).[51]

In addition to serving as a positive T_1 CA for MRI, B-GQDs demonstrate fluorescent property that makes them a marker in optical imaging. Figure S12 (Supporting Information) shows the laser scanning confocal images of SF-763 cells incubated with B-GQDs, acquired under laser irradiation at wavelengths of 405, 488, and 546 nm, respectively. As shwon, B-GQDs produced a bright fluorescence and can illuminate SF-763 cells in multicolor forms. Figure S13 (Supporting Information) shows images of fluorescence, DAPI nuclear stained SF-763 cells after uptaking B-GQDs and excited by a wavelength of 900 nm using two-photon microscopy. This demonstrates that cells can also be illuminated by the upconverted fluorescence emitted by B-GQDs under excitation of NIR laser irradiation. To further investigate applicability of B-GQDs for *in vivo* NIR imaging, nude mice were injected subcutaneously and intravenously with B-CQDs, respectively. As shown in Figure S14 (Supporting Information), fluorescence of B-GQDs can be observed in mice treated with subcutaneous injection of B-GQDs at excitation wavelengths of 670, 710 and 745 nm at both subcutaneous injection sites. The mice treated by intravenous injection of B-GQDs remained emiting NIR fluorescence from liver 24 h post-injection at an excitation wavelength of 710 nm (Figure S15, Supporting Information). Furthermore, NIR signals were observed at an excitation wavelength of 710 nm from various organs of the mice treated with intravenously injected B-CQDs 72 h post-injection (Figure S16, Supporting Information). The PL spectrum of B-GQDs under an excitation wavelength of 710 nm confirmed their NIR emission with a maximum peak at 806 nm (Figure S17, Supporting Information). This result validates their potential use as optical nanoprobes in biomedical imaging.

In summary, we have produced a novel metal-free magnetic carbon material by doping graphene quantum dots (5 nm) with boron atoms. The produced B-GQDs demonstrate a paramagnetic property, and therefore can potentially serve as a CA for T_1 MRI. B-GQDs also exhibit excitation wavelength-tunable photoluminescence property, which allows B-GQDs to serve as a sustainable confocal, two-photon fluorescence, and NIR imaging contrast agent. We demonstrated its biocompatibility and utility for contrast enhancement both in vitro and in vivo. We concluded that this new material may serve as an alternative CA superior to the currently available clinical MRI CAs and provide more reliable diagnostics by cross-validation of the results that are from two imaging modalities but generated with the same contrast material in the same time period.

Supplementary Material

Refer to Web version on PubMed Central for supplementary material.

Acknowledgments

We gratefully acknowledge the financial support from NIHR01CA161953, Seattle Children Hospital, and Kyocera professor endowment. The two photon fluorescence imaging study was supported in part by a gift to the Institute for Stem Cell and Regenerative Medicine at the University of Washington.

References

1. Allemand PM, Khemani KC, Koch A, Wudl F, Holczer K, Donovan S, Grüner G, Thompson JD. Science. 1991; 253:301. [PubMed: 17794696]
2. Makarova TL, Sundqvist B, Hohne R, Esquinazi P, Kopelevich Y, Scharff P, Davydov VA, Kashevarova LS, Rakhmanina AV. Nature. 2001; 413:716. [PubMed: 11607027]
3. Ohldag H, Esquinazi P, Arenholz E, Spemann D, Rothermel M, Setzer A, Butz T. New J Phys. 2010; 12:123012.
4. Soriano D, Leconte N, Ordejón P, Charlier JC, Palacios JJ, Roche S. Phys Rev Lett. 2011; 107:016602. [PubMed: 21797560]
5. Bogani L, Wernsdorfer W. Nat Mater. 2008; 7:179. [PubMed: 18297126]
6. Rao CNR, Matte HSSR, Subrahmanyam KS, Maitra U. Chem Sci. 2012; 3:45.
7. Kikuo H. J Phys Condens Matter. 2001; 13:1295.
8. Lee H, Son YW, Park N, Han S, Yu J. Phys Rev B. 2005; 72:174431.
9. Narymbetov B, Omerzu A, Kabanov VV, Tokumoto M, Kobayashi H, Mihailovic D. Nature. 2000; 407:883. [PubMed: 11057661]
10. Wang Y, Huang Y, Song Y, Zhang X, Ma Y, Liang J, Chen Y. Nano Lett. 2009; 9:220. [PubMed: 19072314]
11. Peng J, Guo Y, Lv H, Dou X, Chen Q, Zhao J, Wu C, Zhu X, Lin Y, Lu W, Wu X, Xie Y. Angew Chem Int Ed. 2016; 55:3176.
12. Esquinazi P, Spemann D, Hohne R, Setzer A, Han KH, Butz T. Phys Rev Lett. 2003; 91:227201. [PubMed: 14683267]
13. Romero-Aburto R, Narayanan TN, Nagaoka Y, Hasumura T, Mitcham TM, Fukuda T, Cox PJ, Bouchard RR, Maekawa T, Kumar DS, Torti SV, Mani SA, Ajayan PM. Adv Mater. 2013; 25:5632. [PubMed: 24038195]
14. Matte HSSR, Subrahmanyam KS, Rao CNR. J Phys Chem C. 2009; 113:9982.
15. Revia RA, Zhang M. Mater Today. 2016; 19:157.
16. Wang H, Zhou S. Biomater Sci. 2016; 4:1062. [PubMed: 27184106]
17. Broome DR. Eur J Radiol. 2008; 66:230. [PubMed: 18372138]
18. Shin TH, Choi Y, Kim S, Cheon J. Chem Soc Rev. 2015; 44:4501. [PubMed: 25652670]
19. Piero S, Caterina C, Silvo A. Curr Med Chem. 2008; 15:1229. [PubMed: 18473815]
20. Kanakia S, Toussaint JD, Chowdhury SM, Lalwani G, Tembulkar T, Button T, Shroyer KR, Moore W, Sitharaman B. Int J Nanomed. 2013; 8:2821.
21. Chen H, Wang GD, Tang W, Todd T, Zhen Z, Tsang C, Hekmatyar K, Cowger T, Hubbard RB, Zhang W, Stickney J, Shen B, Xie J. Adv Mater. 2014; 26:6761. [PubMed: 25178894]
22. Rogosnitzky M, Branch S. Biometals. 2016; 29:365. [PubMed: 27053146]
23. Wang H, Shen J, Li Y, Wei Z, Cao G, Gai Z, Hong K, Banerjee P, Zhou S. Biomater Sci. 2014; 2:915.
24. Wu X, Tian F, Wang W, Chen J, Wu M, Zhao JX. J Mater Chem C. 2013; 1:4676.
25. Hernandez Y, Nicolosi V, Lotya M, Blighe FM, Sun Z, De S, McGovern IT, Holland B, Byrne M, Gun'Ko YK, Boland JJ, Niraj P, Duesberg G, Krishnamurthy S, Goodhue R, Hutchison J, Scardaci V, Ferrari AC, Coleman JN. Nat Nanotechnol. 2008; 3:563. [PubMed: 18772919]

26. Chang YR, Lee HY, Chen K, Chang CC, Tsai DS, Fu CC, Lim TS, Tzeng YK, Fang CY, Han CC, Chang HC, Fann W. Nat Nanotechnol. 2008; 3:284. [PubMed: 18654525]
27. Wang H, Sun Y, Yi J, Fu J, Di J, del Carmen Alonso A, Zhou S. Biomaterials. 2015; 53:117. [PubMed: 25890712]
28. Eda G, Lin YY, Mattevi C, Yamaguchi H, Chen HA, Chen IS, Chen CW, Chhowalla M. Adv Mater. 2010; 22:505. [PubMed: 20217743]
29. Wang H, Di J, Sun Y, Fu J, Wei Z, Matsui H, del Alonso AC, Zhou S. Adv Funct Mater. 2015; 25:5537.
30. Li L, Wu G, Yang G, Peng J, Zhao J, Zhu JJ. Nanoscale. 2013; 5:4015. [PubMed: 23579482]
31. Cao L, Meziani MJ, Sahu S, Sun YP. Acc Chem Res. 2013; 46:171. [PubMed: 23092181]
32. Lee E, Ryu J, Jang J. Chem Commun. 2013; 49:9995.
33. Shen J, Zhu Y, Chen C, Yang X, Li C. Chem Commun. 2011; 47:2580.
34. Sepioni M, Nair RR, Rablen S, Narayanan J, Tuna F, Winpenny R, Geim AK, Grigorieva IV. Phys Rev Lett. 2010; 105:207205. [PubMed: 21231263]
35. Das SK, Bhunia MK, Motin Seikh M, Dutta S, Bhaumik A. Dalton Trans. 2011; 40:2932. [PubMed: 21321735]
36. Kattel K, Park JY, Xu W, Kim HG, Lee EJ, Bony BA, Heo WC, Lee JJ, Jin S, Baeck JS, Chang Y, Kim TJ, Bae JE, Chae KS, Lee GH. ACS Appl Mater Interfaces. 2011; 3:3325. [PubMed: 21853997]
37. Wang Z, Tang C, Sachs R, Barlas Y, Shi J. Phys Rev Lett. 2015; 114:016603. [PubMed: 25615490]
38. Qin S, Guo X, Cao Y, Ni Z, Xu Q. Carbon. 2014; 78:559.
39. Yazyev OV, Helm L. Phys Rev B. 2007; 75:125408.
40. Wang WL, Meng S, Kaxiras E. Nano Lett. 2008; 8:241. [PubMed: 18052302]
41. Radovic LR, Bockrath B. J Am Chem Soc. 2005; 127:5917. [PubMed: 15839691]
42. Young AF, Dean CR, Wang L, Ren H, Cadden-Zimansky P, Watanabe K, Taniguchi T, Hone J, Shepard KL, Kim P. Nat Phys. 2012; 8:550.
43. Nair RR, Sepioni M, Tsai IL, Lehtinen O, Keinonen J, Krasheninnikov AV, Thomson T, Geim AK, Grigorieva IV. Nat Phys. 2012; 8:199.
44. Hu YH. Small. 2014; 10:1451. [PubMed: 24376224]
45. Panich M, Shames AI, Nakajima T. J Phys Chem Solids. 2001; 62:959.
46. Höhne R, Esquinazi P, Heera V, Weishart H, Setzer A, Spemann D. J Magn Magn Mater. 2008; 320:966.
47. Chen F, Bu W, Zhang S, Liu J, Fan W, Zhou L, Peng W, Shi J. Adv Funct Mater. 2013; 23:298.
48. Xu Y, Jia XH, Yin XB, He XW, Zhang YK. Anal Chem. 2014; 86:12122. [PubMed: 25383762]
49. Gong N, Wang H, Li S, Deng Y, Chen Xa, Ye L, Gu W. Langmuir. 2014; 30:10933. [PubMed: 25157595]
50. Stephen ZR, Kievit FM, Veiseh O, Chiarelli PA, Fang C, Wang K, Hatzinger SJ, Ellenbogen RG, Silber JR, Zhang M. ACS Nano. 2014; 8:10383. [PubMed: 25247850]
51. Kim BH, Lee N, Kim H, An K, Park YI, Choi Y, Shin K, Lee Y, Kwon SG, Na HB, Park JG, Ahn TY, Kim YW, Moon WK, Choi SH, Hyeon T. J Am Chem Soc. 2011; 133:12624. [PubMed: 21744804]

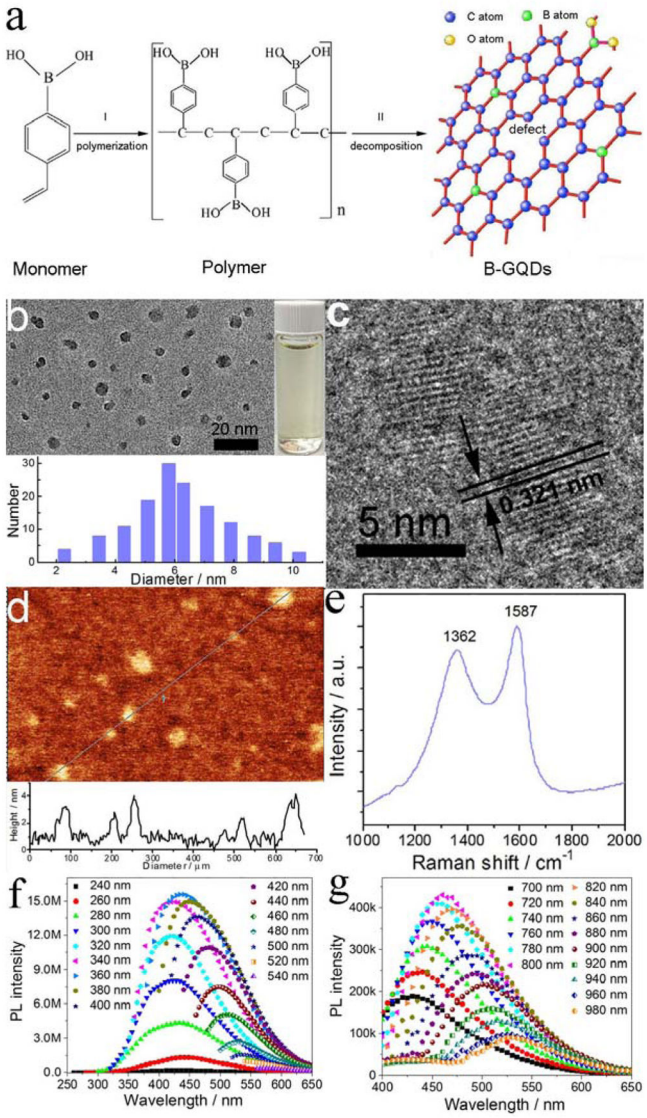

Figure 1.

Formation, structure and PL property of B-GQDs. (a) The schematic representation of the formation of B-GQDs. (b) TEM image and size distribution, (c) lattice fringe, (d) atomic force microscopy image, (e) Raman spectrum, (f) PL spectra and (g) upconverted PL spectra of B-GQDs.

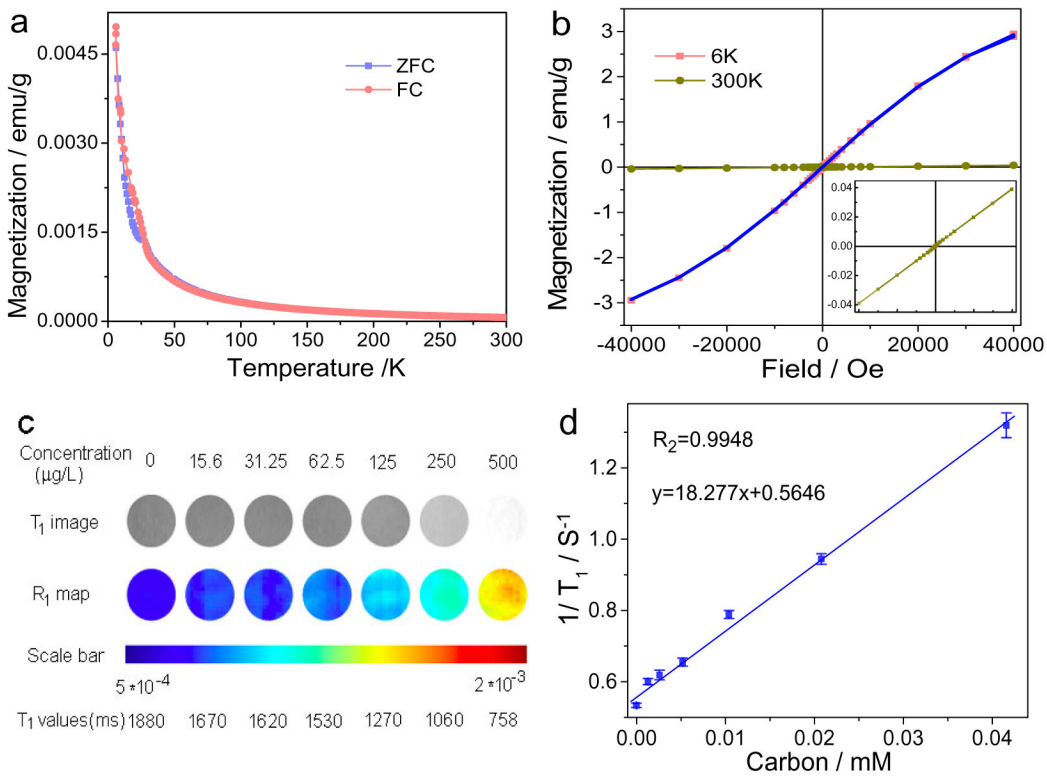

Figure 2.

Magnetic properties and in vitro MRI of the B-GQDs. (a) Zero-field-cooling curves of B-GQDs measured in an applied field of 50 Oe. (b) Magnetization hysteresis loops of the B-GQDs at 6 K and 300 K in the range of −40 kOe < H < +40 kOe. The blue curve is the Brillouin function fitting of the 6K hysteresis curve. The inset is the enlarged magnetization hysteresis loop of B-GQDs at 300 K. (c) T_1-weighted MR images and R_1 maps of MRI phantom images of B-GQDs at different B-GQD concentrations. (d) Plot of $1/T_1$ as a function of B-GQD concentration. The slope of the curve is defined as the specific relaxivity of r_1.

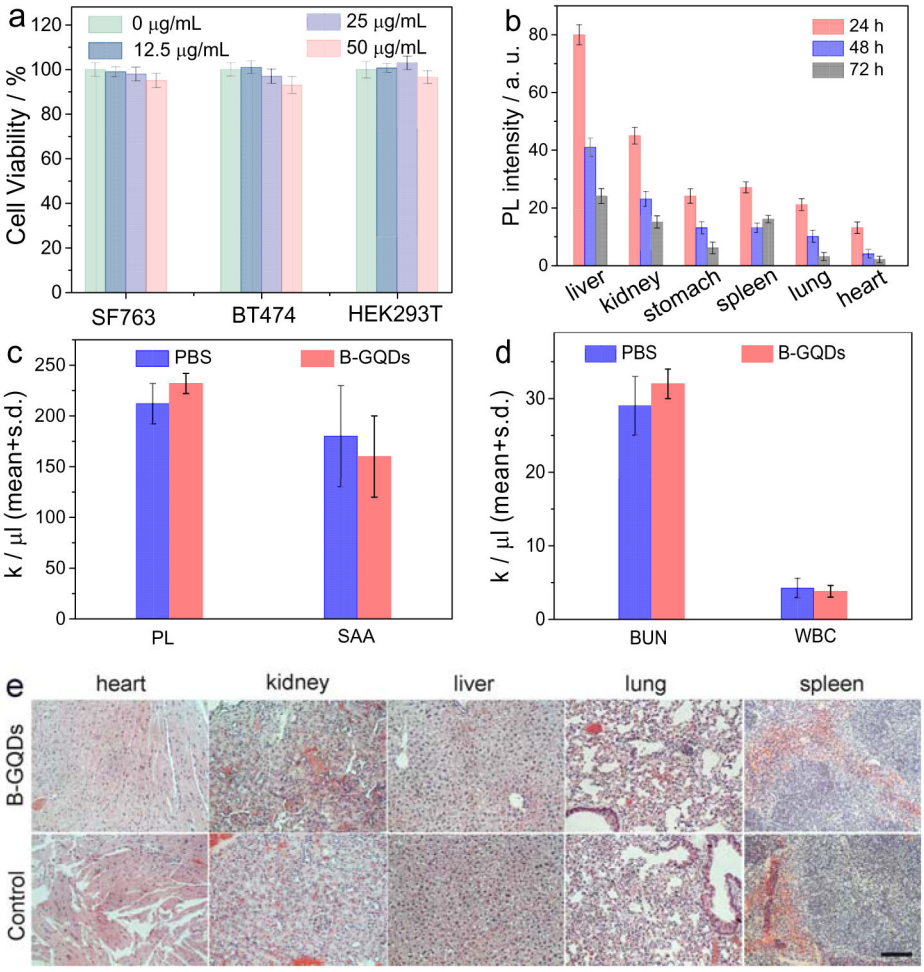

Figure 3.

In vitro and *in vivo* biocompatibility assessment of B-GQDs. (a) In vitro cytotoxicity study of B-GQDs performed by assessing the viability of SF763, BT474 and HEK293T cells 72 h after treatment with B-GQDs. (b) Distributions of B-GQDs in various organs and tissues of nude mice receiving B-GQDs, determined at various time points post-injection. Assessment of toxic effects of B-GQDs on liver and kidney by hematology analysis. (c) platelet (PL) levels and serum alanine aminotransferase (SAA) levels, (d) blood urea nitrogen levels (BUN) and white blood (WBC) cells of mice receiving B-GQDs or PBS injection, measured 24 h after administration (standard deviation of mean, n = 4 mice per treatment). (e) H&E stained tissue sections of mouse heart, kidney, liver, lung and spleen, obtained from non-injected animals (bottom row, control) and those injected with B-GQDs at a concentration of 1 mg mL^{-1} (top row). The scale bar is 125 μm.

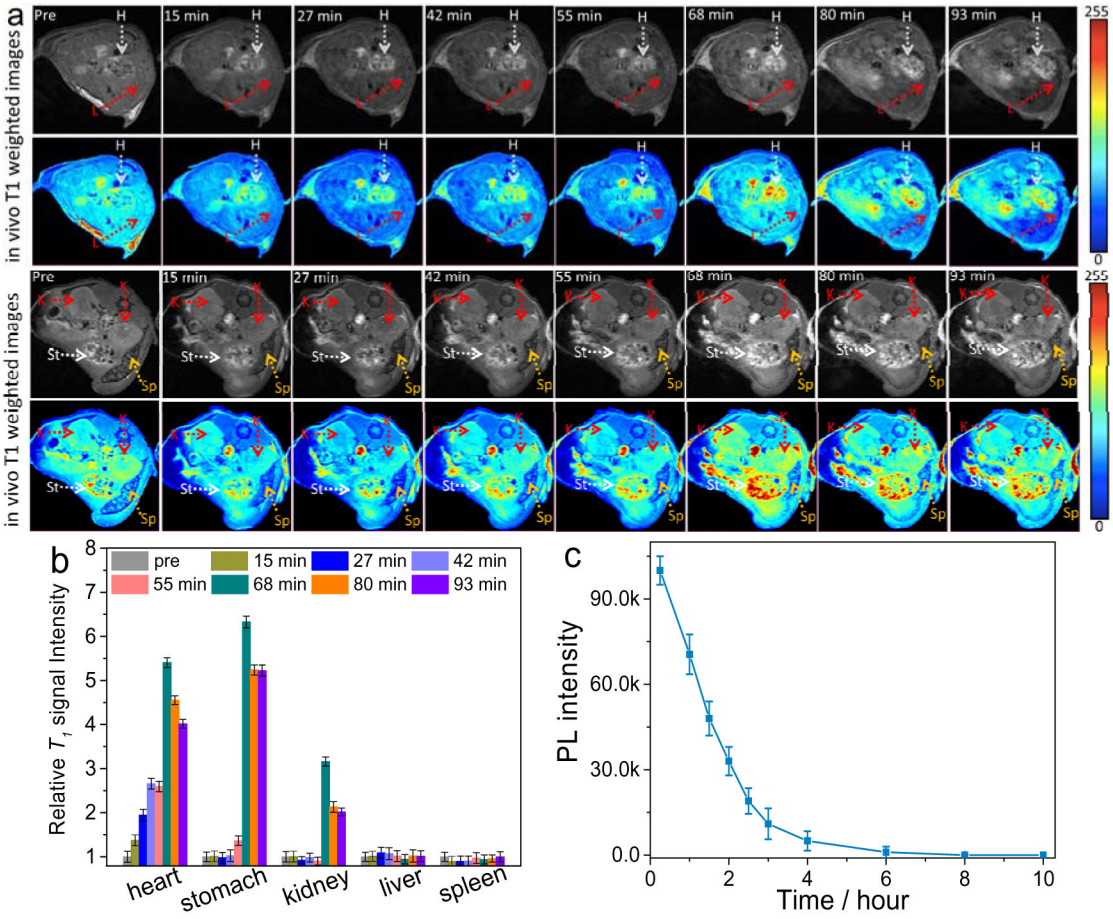

Figure 4.

In vivo MRI of mice receiving B-GQDs. (a) *In vivo* T_1-weighted MR images of the cross-sections of mice receiving B-GQD treatment with dynamic time-resolved MRI acquired at various time points after intravenous administration. The arrows denote various organs: heart (H), liver (L), kidneys (K), spleen (Sp) and stomach (St). (b) Relative T_1 signal intensity variation in mice injected intravenously with B-GQDs with dynamic time-resolved MRI acquired from organs of interest before and at different time points after administration. (c) Blood half-life of the B-GQD determined by fluorescence measurements. Each data point is acquired from three animals in a group.